

Molecular dynamics simulation of methane transport in confined organic nanopores with high relative roughness



Jian He^{a,b}, Yang Ju^{a,c,*}, Karol Kulasinski^d, Liange Zheng^d, Laura Lammers^e

^a State Key Laboratory for Geomechanics & Deep Underground Engineering, China University of Mining and Technology, No. 1 University Avenue, Xuzhou, 221116, China

^b Energy Geosciences Division, Lawrence Berkeley National Laboratory, Berkeley, CA, 94720, USA

^c State Key Laboratory of Coal Resources and Safe Mining, China University of Mining and Technology at Beijing, D11 Xueyuan Road, Beijing, 100083, China

^d Earth & Environmental Sciences Area, Department of Geochemistry, Lawrence Berkeley National Laboratory, Berkeley, CA, 94720, USA

^e Department of Environmental Science, Policy, and Management, University of California, Berkeley, USA

ARTICLE INFO

Keywords:

Gas transport
Nanopores
Relative roughness
Molecular dynamics
Slip flow
Adsorption

ABSTRACT

Understanding and characterizing the transport of shale gas (methane) through the nanopores of kerogens are critical for the accurate prediction of shale gas recovery. However, the key factors that regulate shale gas transport through highly roughened nanopores of shale kerogens are not fully understood. In this work, methane transport in organic nanopores with a high relative roughness is characterized using equilibrium and non-equilibrium molecular dynamics methods. According to our results, the CH_4 mass flux has a linear relationship with the pressure gradient, consistent with previous studies, while the calculated slip lengths and gas fluxes varied with different roughness geometries in the order of sigmoidal \geq triangular $>$ rectangular. Surface slip flow can be a major contributor to the overall gas flux, but surprisingly, the relative contribution of surface slip flow is independent of the pressure gradient. In contrast, the contributions of both slip flow and the average gas fluxes vary strongly with pore diameters. Typical contributions of the adsorbed layer to the overall gas flux are in the range 20–40% but vary from as high as 74% in a 4-nm pore to as low as 6% in a 16-nm pore. Compared to smooth nanopores, we find that, in nanopores with realistically high degrees of relative roughness, methane confinement in cavities decouples slip flow from the flow in the pore interior, significantly reducing the overall flux.

1. Introduction

Owing to the technological innovations in hydraulic fracturing and horizontal drilling, shale resources have become one of the most important modern energy resources. The key challenge in exploiting shale gas resources is the very low permeability of the fine-grained sedimentary reservoirs that host shale gas, which can be as low as 0.24 nD (Chalmers et al., 2012b; Dong et al., 2015). The pore system in these shales is dominantly at the scale of nanometers (Loucks et al., 2009). Nanopores with a size of < 30 nm can make up as much as 80% of the very limited total shale porosity, which is in the range of 2%–7% for some North American gas shales (Chalmers et al., 2012a; Kaufhold et al., 2016). However, some prior experiments have indicated that shale gas transportation in highly roughened nanopores in kerogen is different from that in smooth nanopores (Chae and Huang, 2016; Javadpour et al., 2015). The physics regulating shale gas transport in highly roughened kerogen nanopores and the relationship between

nanostructure roughness and gas-flow state is not fully understood.

Because of the molecular-scale nature of the system, molecular simulations including molecular dynamics (MD) and grand canonical molecular dynamics (GCMC) simulations have been used to analyze nanoscale gas flows (Firouzi and Wilcox, 2013; Sui and Yao, 2016; Kazemi and Takbiri-Borujeni, 2016b). Particularly, the effect of adsorption and pressure gradients on the gas flow in smooth nanopores of variable diameter has been deeply probed using molecular simulation methods. It was reported that shale gas flux increased from 4498 to 37244 $\text{kg m}^{-2} \text{s}^{-1}$ as the pressure gradient increased from 1.8 to 17.65 kPa nm^{-1} in a 2-nm-slit organic nanopore and that the contribution of the adsorbed molecules can be $> 50\%$ of the total mass flux of the channel (Kazemi and Takbiri-Borujeni, 2016a, c). With the increase of pore sizes, the proportion of adsorbed gas decreased to $< 40\%$ in a 10-nm-slit organic pore. For inorganic pores, the contribution of the adsorption layer can almost be neglected (Wu and Zhang, 2016).

In addition to adsorption and pressure gradients (Jin and

* Corresponding author. State Key Laboratory of Coal Resources and Safe Mining, China University of Mining and Technology at Beijing, D11 Xueyuan Road, Beijing, 100083, China.

E-mail address: juy@cumtb.edu.cn (Y. Ju).

Firoozabadi, 2015; Skoulidas et al., 2002), roughness is an important factor impacting fluid flux through micropores and nanopores. In rough inorganic nanopores, gas properties including density, transport, and structure vary significantly as functions of distance from the pore wall (Jiang et al., 2017), and the boundary conditions including the slip length are related to not only the Knudsen number ($Kn = \lambda/l$, where l is the characteristic size of nanopores and λ is the mean free path of molecules) (Wu and Zhang, 2016) but also the surface roughness (Cao et al., 2006; Noorian et al., 2013). Apart from simulations, the influence of roughness on the fluid flow in nanopores has been experimentally measured. A slip length of $> 20\text{ }\mu\text{m}$ was obtained in an ultra-hydrophobic surface covered with microridges (Ou et al., 2004). However, even the heterogeneities of the monolayer obtained from the self-assembly method are sufficient to eliminate the slippage (Pit et al., 2000; Schmatko et al., 2006), which implies that the nanoscale fluid flow is very sensitive to roughness.

A few prior studies have illustrated that gas flow through nanochannels is controlled by a complex interplay among gas adsorption, absolute roughness, and roughness geometry (Cao et al., 2006; Noorian et al., 2013; Rahmatipour et al., 2017; Xie and Cao, 2016). Most of these investigations focused on modelling flow in pores with a low relative roughness ($< \sim 5\%$). Nevertheless, kerogen in shale is an intrinsically complex material composed of an amorphous porous carbon skeleton with pore sizes in the range of a few angstroms to micrometers (Bousige et al., 2016), and the height of rough units of asperities in the nanopores is comparable to the molecular mean free path (MFP) (Chae and Huang, 2016). It was reported (Javadpour et al., 2015) that the height of rough units in organic matter (OM) nanopores in shale reached $\pm 38\text{ nm}$ with a roughness of tens of nanometers, while the relative roughness (defined as $R_r = h/D$, where h is the height of rough units and D is the pore size) can be as high as 25%. The relative roughness of nanopores in shale is typically much higher than that for macroscale pores ($R_r \sim 5\%$, characterized by a Moody chart) (Moody, 1944).

Shale gas flow at the nanoscale is very sensitive to the magnitude of relative roughness (Pit et al., 2000; Schmatko et al., 2006), which not only dramatically impacts shale gas production, but also affects the migration mechanism of gas in nanopores (Castex et al., 2017). Despite this fact, shale gas flow in nanopores with a high relative roughness ($> 5\%$), typical of shale nanoporosity, has not been previously investigated. In this paper, we use equilibrium and non-equilibrium MD simulations to study methane flow through graphite pores, which serves as an idealized representation of a kerogen nanopore system, to better understand and characterize the variation of shale gas transport with changing relative roughness. The effects of relative roughness, roughness geometries, and pressure gradients on shale gas flux in nanopores with a high relative roughness are all discussed. The relative contributions of surface and bulk transportation to the overall gas flux are calculated, providing a realistic representation of CH_4 transport in a kerogen pore system.

2. Models and methods

2.1. Rough nanopore simulation setup

Graphite sheets are used to represent the walls of a kerogen pore system in shale (Kazemi and Takbiri-Borujeni, 2016a). Several rough surfaces of different geometries are constructed from graphite fragments cut from graphite sheets. For the rectangular model, the length of a single fragment along the x-direction is kept the same as those of the sinusoidal and triangular models (represented with $M = 2.2\text{ nm}$ in Fig. 1). For the sinusoidal model, the obtained flat fragments are first placed between the slit graphite nanopores with an inclination of 45° .

Then, the structure is equilibrated with an MD simulation, and the fragments are deformed. Several sinusoidal graphite fragments are exported, and we choose the most appropriate one by keeping the length of fragments in the x-direction equal to 2.2 nm and the height of asperities equal to 1 nm . A typical simulation cell with triangular asperities is illustrated in Fig. 1. To improve computational efficiency, we used coarse-grained particles to represent gases moving like particles with zero charge. Therefore, the effect of Coulomb interactions between the gases and the wall on the fluid transportation is ignored, and the effect of dangling and/or broken bonds is weak and also ignored here (Legesse et al., 2016; Gao et al., 2017). A buffer distance of 2.5 \AA is set between each pair of graphite fragments to allow relaxation of the sheets while preventing direct overlap. This buffer distance is greater than the bond length of carbon but sufficiently small to prevent methane molecules from entering gaps between the graphite fragments (Kazemi and Takbiri-Borujeni, 2016b).

Nanopore diameters are varied by setting the maximum distance (D) between the two walls to $4, 8, 12$, and 16 nm to study the influence of pore size on shale gas flow. The heights of the rough units are $h = 2, 1, 0.65$, and 0.5 nm , which correspond to relative roughness values, R_r , of $25\%, 12.5\%, 8.33\%$, and 6.25% , respectively. The absolute surface roughness (R_a) distribution is defined as the ratio of roughness height to the periodicity (P in nm) of the rough units ($R_a = h/P$). With increasing periodicity, R_a decreases for a constant R_r . In this paper, roughness periodicities of $2.9, 4.35$, and 8.7 nm are used. The box dimensions in the x (parallel to flow) and y (perpendicular to flow) directions are set to 8.7 and 4.3 nm , respectively. In accordance with a typical shale gas reservoir condition (Yan et al., 2017), a temperature of 330 K is set and controlled by a thermostat. Consequently, the density of methane at 0.1312 g/cm^3 is used as the initial condition, as derived from the National Institute of Standards and Technology's (NIST's) database (2011) for a bulk pressure of 20 MPa (Shen et al., 2011).

2.2. Simulation methods

MD simulations are generally performed using fast parallel algorithms for short-range MD, such as LAMMPS, which is a powerful open-source software for molecular simulations (Plimpton, 1993). Visual MD (Humphrey et al., 1996) and OVITO (Stukowski, 2010) are used for visualization, and the obtained data are processed using a custom Python code (Oliphant, 2007). The 12-6 Lennard-Jones potential is used to calculate van der Waals interactions with a cutoff distance of 12 \AA (Kazemi and Takbiri-Borujeni, 2016b). The OPLS-AA force field is used to describe graphite interactions, and individual CH_4 molecules are modeled as single coarse-grained particles using the force-field parameters listed in Table 1. This method is often used to simplify the model and reduce the computation time while maintaining a relative error of $< 5.2\%$ (Wang et al., 2016b; Wu et al., 2015). The graphite layers are fixed during the simulation. All MD simulations are performed with a constant number of particles (N) at a constant volume (V) and temperature (T). The simulation temperature of 330 K is controlled with a Nose-Hoover thermostat (Evans and Holian, 1985).

The MD simulations are divided into two stages: equilibrium MD (EMD) simulation and non-equilibrium MD (NEMD) simulation. EMD is used to equilibrate the system and collect equilibrium information in the absence of pressure gradients. The structure is relaxed for 1 ns using a time step of 1 fs , following which the simulation is conducted for another 1 ns to collect trajectories. The trajectories of CH_4 are collected every 1 ps . For the NEMD simulation, an additional force is added to every CH_4 particle parallel to the x direction to mimic pressure gradients in the nanopore. Meanwhile, the temperature is controlled only by the velocity component in the y direction, which is perpendicular to the direction of the additional force (Wang et al., 2016a).

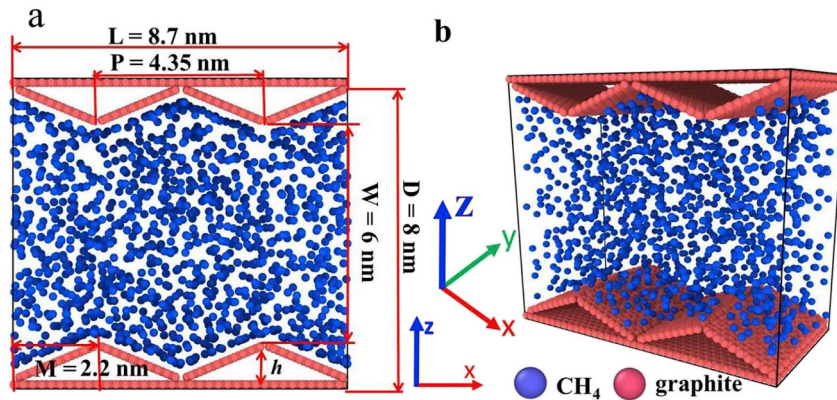


Fig. 1. Snapshots of the simulation box: (a) front view; (b) side view. Blue and red particles represent methane and graphite layers, respectively.

Table 1
Force-field parameters of graphite and methane used in this simulation.

Atom type	ϵ (kcal·mol ⁻¹)	σ (Å)
methane	0.294	3.73
graphite	0.07	3.55

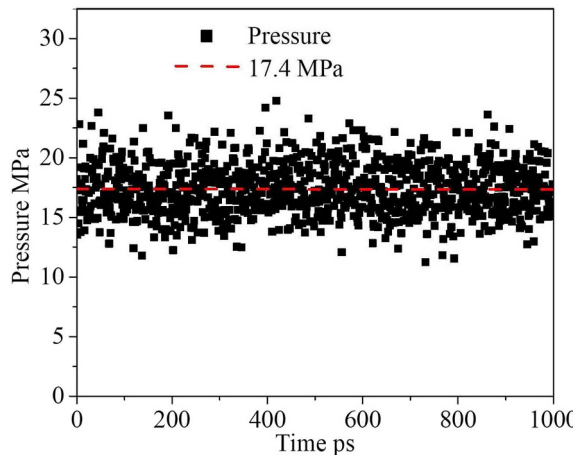


Fig. 2. Local pressure of CH₄ in the bulk phase calculated with the Green–Kubo equation and fitted with a red straight line parallel to the x axis.

To obtain the real pressure inside pores, the local CH₄ pressure in pores is calculated via EMD simulation. Fig. 2 illustrates the results from the last 1 ns. Because the nanopores are confined, the pressure varies dramatically from 12 to 25 MPa according to the simulation. We fitted the pressure with a straight line and found that the average pressure is 17.4 MPa, which is slightly less than the pressure of the idealized shale gas reservoir. This is mainly caused by the adsorption of the graphite walls; the density in the bulk phase is less than the standard value from the NIST database (Shen et al., 2011).

In NEMD simulations, the equilibration time is extended to 5 ns, followed by a 10-ns production run with CH₄ trajectories collected again every 1 ps. Because of the presence of the rough surface, it is inaccurate to average the data in layers perpendicular to the z direction. Instead, we divide the nanopore into small bins of 1 Å on a side along x and z . The collected data in each small bin are averaged over the simulation time. The average densities $\hat{\rho}_{i, i \in m, bin}$ and velocities $\hat{v}_{i, i \in m, bin}$ in the i_{th} bin over j ps are calculated using the following expressions:

$$\hat{\rho}_{i, i \in m, bin} = \frac{\sum_{j \in N} m_{ij}}{N \cdot \Delta x \cdot \Delta z \cdot Ly'} \quad (1)$$

$$\hat{v}_{i, i \in m, bin} = \frac{\sum_{j \in N} m_{ij} v_{ij}}{N \cdot \sum_{j \in N} m_{ij}}, \quad (2)$$

where N is the total number of trajectories collected from the MD production run (where $N = 1000$ for EMD and $N = 10,000$ for NEMD); m_{ij} and v_{ij} are the mass in grams and the velocity in Åfs⁻¹, respectively; Ly is the length of the simulation cell in the y direction in Å; and Δx and Δz are the widths of the bins in the x and z directions in Å, respectively.

2.3. Flux and viscosity calculations

For our simulations, the methane volumetric flux J_f in m·s⁻¹, which can be converted into mass flux by multiplying it by the bulk phase density, is modeled using the Hagen–Poiseuille (HP) equation modified to include a slip effect (Jin and Firoozabadi, 2015; Wang et al., 2016b):

$$J_f = -\frac{nFw^2}{12\eta} \left(1 + \frac{6L_s}{w} \right), \quad (3)$$

where L_s is the slip length in Å obtained from the fitting process, F is the external force applied to the CH₄ molecules in kcal·mol⁻¹Å⁻¹, n is the density of gas molecules in mol·cm⁻³, w is the effective width of the pore at the calculated points in Å, and η is the viscosity of the flow in Pas. There are two ways to calculate the viscosity. One is through velocity fitting with the HP equation (Eq. (4)). The velocity is fitted with a parabolic equation $v = az^2 + c$, and the viscosity is subsequently calculated from $\eta = -nF/(2a)$, following which L_s can be calculated with c (Wang et al., 2016c):

$$\bar{v} = -\frac{nF}{2\eta} \left(z^2 - \frac{w^2}{4} - wL_s \right). \quad (4)$$

Alternatively, dynamic viscosity can be calculated from the Green–Kubo (GK) equation (Mondello and Grest, 1997):

$$\eta = \frac{V}{10k_B T} \int_0^\infty \left(\sum_{\alpha\beta} P_{\alpha\beta}(0) P_{\alpha\beta}(t) \right) dt, \quad (5)$$

where k_B is the Boltzmann constant (1.38×10^{-23} m² kg·s⁻²K⁻¹), T is the temperature in kelvin, V is the volume in Å³, and $P_{\alpha\beta}$ is the symmetric component of the stress tensor σ :

$$P_{\alpha\beta} = \frac{1}{2} (\sigma_{\alpha\beta} + \sigma_{\beta\alpha}) - \frac{1}{3} \delta_{\alpha\beta} \left(\sum_y \sigma_{yy} \right). \quad (6)$$

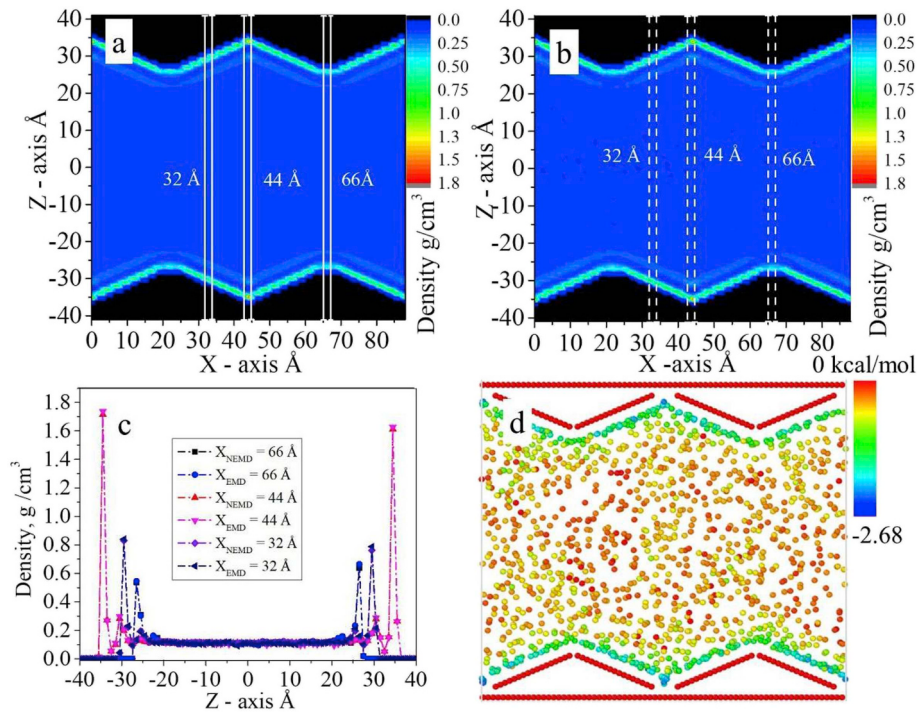


Fig. 3. Density distribution maps in (a) NEMD and (b) EMD simulations. (c) Density profiles at $x = 3.2, 4.4$, and 6.6 nm represented in different colors. (d) Snapshot of the potential-energy distribution of methane in nanopores after the NEMD simulation.

The viscosity values obtained from these two methods are compared to determine the fitting method and theory most suitable for the simulations.

3. Results and discussion

3.1. Density distribution in roughened nanopores

A nanopore with a relative roughness of 12.5% and a triangular roughness geometry was chosen to investigate the methane density distribution. An external force of $0.001 \text{ kcal mol}^{-1} \text{ Å}^{-1}$ was used as the pressure gradient to push the CH_4 flow in the x direction in the NEMD simulation. Fig. 3(a)–3(c) show the corresponding CH_4 density map. It is known that methane tends to accumulate on graphite nanopore walls, forming an adsorbed layer on the surface (Tang et al., 2017). The density distribution of CH_4 is nearly the same for both the EMD and NEMD simulations in the center (bulk) and near-surface regions of the pore. The density in the center area is constant at 0.1132 g/cm^3 , which is less than the pore-averaged density (0.1312 g/cm^3) owing to the excess methane adsorption on the graphite walls. In the center region, the interactions of methane particles with the wall are much less significant than interparticle interactions; thus, the density is evenly distributed, and the effect of the wall surface can be ignored.

Nearer to the wall, the methane density rapidly increases, indicating the formation of an adsorbed layer. According to the density distribution in Fig. 3(c), the density at the location closest to the wall ($x = 44 \text{ Å}$) is higher than that at any other location in the simulation cell. Along the surface of the triangular roughness units, the density of the adsorption layer decreases towards the apex ($x = 66 \text{ Å}$), which is also the narrowest part of the pore. The density at the bottom point reaches 1.73 g/cm^3 , while, at the apex of the triangle, the density decreases to 0.65 g/cm^3 . In the middle of triangle surface ($x = 32 \text{ Å}$), the density is 0.9 g/cm^3 . The formation of two distinct layers of adsorbed methane is observed in both the density profiles and density maps. The

total thickness of the two adsorption layers is $\sim 8 \text{ Å}$, which is approximately twice the size of the simulated methane molecule (Greathouse et al., 2015; Wang et al., 2016a). The distance between the first density maximum and the wall is $\sim 3.5 \text{ Å}$, which corresponds to the hard sphere radius of our coarse-grain methane, as determined by the Lennard-Jones interaction (Wang et al., 2018). The accumulation of CH_4 is ascribed to the attractive potential between the methane and the pore walls (Wu et al., 2015). Fig. 2(d) depicts a snapshot of the potential-energy distribution of methane in the nanochannel obtained after 15 ns of the NEMD simulation. As shown in the figure, the potential-energy minimum for methane adsorption ($-2.78 \text{ kcal mol}^{-1}$) coincides with the corner between two rough units, where methane is more completely coordinated by the carbon surface (Wu et al., 2015). The calculated potential energies agree well with the measured densities, wherein the highest density regions along the pore wall correspond to the lowest-free-energy regions, indicating that the system is equilibrated with respect to the potential of the mean force. The methane in the bulk interior area of the pores has a higher and uniform potential energy, resulting in a lower and uniform density in this region. Consequently, methane can freely move in the bulk region owing to negligible surface interaction (Sharma et al., 2014; Li et al., 2016).

3.2. Flow characterization

3.2.1. Velocity distribution

Fig. 4(a) shows the obtained velocity profiles across the pore at $x = 3.2, 4.4$, and 6.6 nm. Gas transport in pores of similar diameter ($\sim 1\text{--}10 \text{ nm}$) tends to fall within a transitional flow regime dominated by Knudsen diffusion and/or slip flow over a wide range of pressures (Yao et al., 2013). To determine whether the HP model with a slip term is still suited to this situation, the viscosity of CH_4 is calculated using two different methods and compared with the NIST data and the Green-Kubo equation (Mondello and Grest, 1997), as well as the modified HP equation. The result is shown in Fig. 4(b).

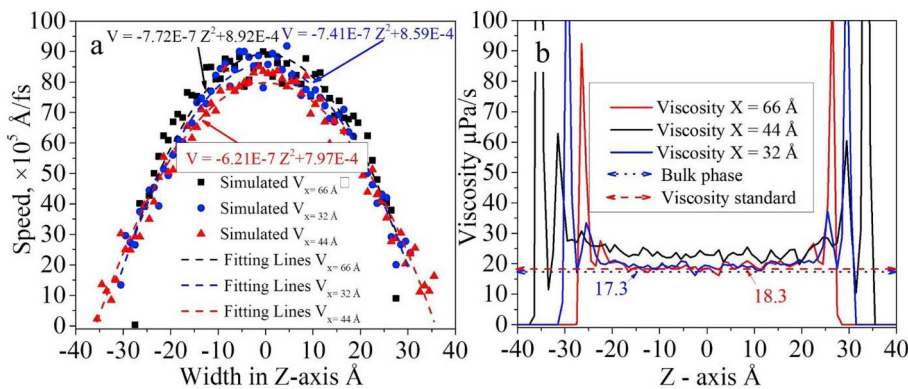


Fig. 4. (a) Velocity profiles (solid samples) and corresponding fitting lines (dashed lines) at $x = 3.2, 4.4$, and 6.6 nm obtained with the unconstrained modified HP equation. (b) Comparison between viscosity calculated from the modified HP equation (solid lines) and the real viscosity of $17.3 \mu\text{Pa s}$ calculated with MD simulation.

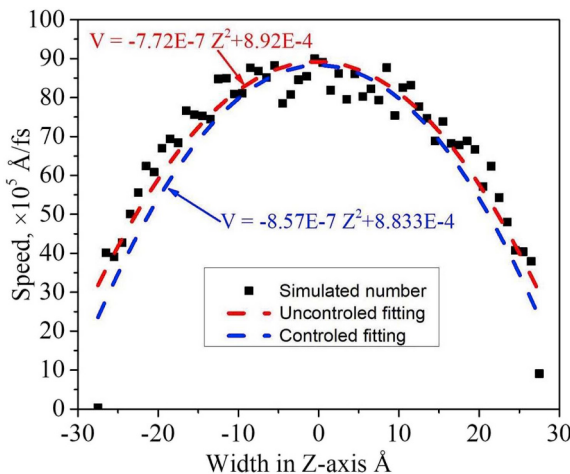


Fig. 5. Velocity profiles and corresponding fitting lines at $x = 6.6 \text{ nm}$ with controlled-parameter (green dashed line) and uncontrolled-parameter (red dashed line) HP fittings.

We calculate viscosity using the modified HP equation by solving Eq. (4) with a parabolic fit to the velocity profile, $v = (-7.72 \times 10^{-7}) z^2 + 8.92 \times 10^{-4}$, as shown in Fig. 4. The obtained viscosity of the adsorbed gas layer is $> 100 \mu\text{Pa s}$, which is much higher than that of the bulk region of the pore (Fig. 4(b)). The bulk methane viscosity we calculated from the HP equation is $19.1 \mu\text{Pa s}$, which is slightly higher than the average viscosity obtained from the GK equation ($17.3 \mu\text{Pa s}$), as represented by the dashed line in Fig. 4(b). For this method, the viscosity in the bulk interior region of the nanopore is the same as the viscosity of a bulk-phase fluid at the same pressure, 17.4 MPa . The use of the uncontrolled HP equation provides reasonable estimates of methane viscosity in the nanopore, with values slightly higher than the standard value obtained from the GK equation.

The overestimation of viscosity by the uncontrolled HP method may

be caused by two factors: (1) the ultra-low friction of the graphite fragment and (2) unconstrained parameter fitting. Usually, gas flow in smooth parallel graphite nanopores tends to occur as plug flow, as reported by many researchers (Jin and Firoozabadi, 2015; Kazemi and Takbiri-Borujeni, 2016a; Wu and Zhang, 2016). Similar phenomena were observed in this study.

The differences between uncontrolled and controlled fitting results are analyzed using the modified HP equation (see Fig. 5). In the parameter-controlled fitting method, the parameter a in the equation $v = az^2 + c$ is set as -8.57×10^{-7} , which is obtained from the equation $a = -nF/2\eta$ at a real viscosity equal to $17.3 \mu\text{Pa s}$. The R-square fitting is ~ 0.839 . According to the controlled HP equation, the slip length and flux both decreased. The velocity based on the parameter-uncontrolled fitting method is smaller than the simulated velocity. Therefore, we used the parameter-uncontrolled fitting results to evaluate the methane flow in high-relative-roughness nanopores.

To evaluate the errors of the calculation, we fitted the velocity profiles with the modified HP equation, following which the flux, viscosity, and friction coefficient are obtained as listed in Table 2. The average flux was calculated with the equation $f_2 = (\sum_{i \in m, bin} \hat{\rho}_i \hat{v}_i)/m$, where $m = 56$. Comparison of the fluxes obtained from the two different methods shows that f_{HP} is always less than f_2 , which implies that the modified HP equation may underestimate the real flux by $\sim 12\%$. This has been reported previously in many papers on the flow in smooth graphite nanopores (Jin and Firoozabadi, 2015; Jin and Firoozabadi, 2016; Suk and Aluru, 2013). Some researchers have attempted to introduce an apparent permeability coefficient to correct the HP equation (Islam and Patzek, 2014; Such et al., 2016). We noticed that shale gas flow in roughened nanopores exhibited a parabolic velocity profile, which is a distinct characteristic of viscous flow (Kou et al., 2016). According to previous studies, the flow model still belongs to the slip flow region (Such et al., 2016; Yao et al., 2013). Therefore, the HP equation with a slip term can be used to evaluate the effect of relative roughness on the gas flux. The result also shows that the modified HP equation can yield the viscosity in this situation with an error ranging from 5.2% to 12.7% (Table 2).

Table 2

Obtained shale gas properties from the modified HP equation in different rough OM pores with an external force at $0.001 \text{ kcal mol}^{-1} \text{\AA}^{-1}$ and a temperature of 330 K .

	Slip length (\AA)	f_{HP} ($\text{kg/m}^2\text{s}$)	f_2 ($\text{kg/m}^2\text{s}$)	Flux errors	Viscosity (Pa s)	Viscosity errors	Friction coefficient ($\text{N}\cdot\text{s}/\text{m}^3$)
Rectangle	1.17	5.73×10^3	6.50×10^3	11.8%	1.82×10^{-5}	5.2%	1.55×10^5
Sigmoidal	6.97	8.27×10^3	9.53×10^3	13.2%	1.95×10^{-5}	12.7%	2.80×10^4
Triangle	6.62	7.82×10^3	8.86×10^3	11.7%	1.91×10^{-5}	10.4%	2.88×10^4

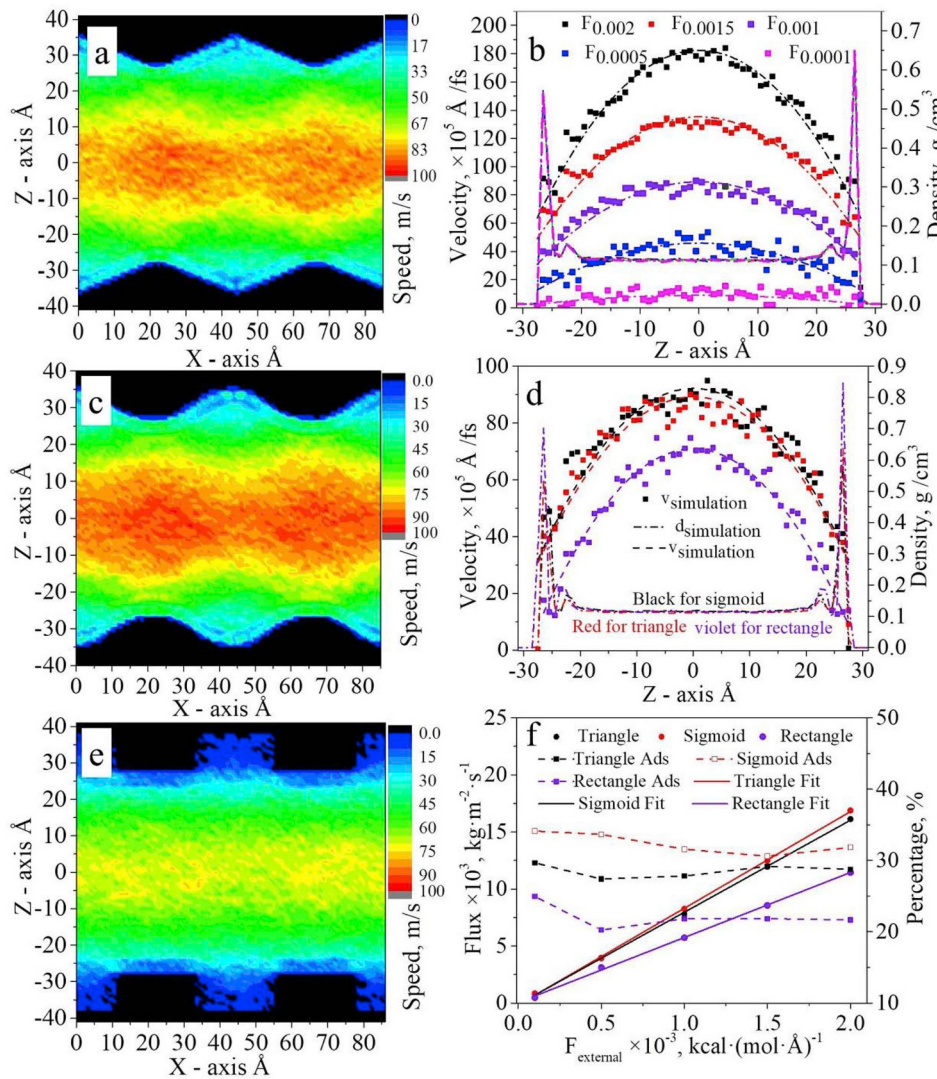


Fig. 6. Velocity distribution maps in nanopores with (a) sigmoidal, (c) triangular, and (e) rectangular asperities on the wall at an external force of 0.001 kcal mol⁻¹ Å⁻¹. (b) Velocity and density profiles (dash-dotted lines) at the narrow points in nanopores with triangular asperities at external forces ranging from 0.0001 to 0.002 kcal mol⁻¹ Å⁻¹. (d) Velocity and density profiles with different rough units at an external force of 0.001 kcal mol⁻¹ Å⁻¹. (f) Molecular flux at different pressure gradients in nanopores with different surface structures (solid lines) and the contribution of the adsorption layer to the average molecular flux (dashed lines).

3.2.2. Impacts of pressure gradient and roughness geometry on gas flux

Flux is an important factor to be evaluated during shale gas production. In this section, we evaluate the shale gas flow flux in a roughened organic nanopore under a range of pressure gradients. The applied external force F is set to 0.0001, 0.0005, 0.001, 0.0015, and 0.002 kcal mol⁻¹ Å⁻¹ in these simulations, similar to values in previous studies (Docherty et al., 2013; Wang et al., 2016c). The pressure gradients are calculated from the external applied force based on (Docherty et al., 2013; Kazemi and Takbiri-Borujeni, 2016c)

$$nF = \frac{\partial P}{\partial L} = \frac{P_1 - P_2}{L}. \quad (7)$$

For example, an external force of 0.001 kcal mol⁻¹ Å⁻¹ results in a pressure gradient of 0.3159 MPa nm⁻¹. This extremely high pressure gradient is necessary to allow the MD simulations to reach a steady state within a reasonable time (Kannam et al., 2012; Yen, 2013).

The resulting velocity and density profiles for methane along the z axis at the narrowest point in the pore are plotted in Fig. 6 for different roughness geometries and pressure gradients. With increasing pressure gradient, the velocity across the pore increases rapidly (Fig. 6(b)). The distribution of velocity profiles across the z axis exhibits a parabolic shape, which is an important characteristic of viscous flow (Kou et al., 2016). The maximum speed at the center of the channel is higher than

the speed near the surface by a factor of nearly 2–3. This is mainly ascribed to the high relative roughness of the surface, which causes a dramatic speed decrease from the center to the surface. The viscosity obtained from the modified HP equation in the center area with increased external force is ~17.2–19.5 μPa s.

In addition to pressure effects, the roughness geometry (i.e. triangular, sigmoidal, or rectangular asperities) has a significant impact on shale gas transport. The velocity distribution maps of whole pores at an external force of 0.001 kcal mol⁻¹ Å⁻¹ are shown in Fig. 6 (a), 6(c), and 6(e). The velocity at the narrowest points is higher than that at the wider area along the same z axis. This is reasonable because the flow rate and particle numbers are kept constant during the simulation. The friction coefficients (λ) from the nanopore wall can be calculated using the relation $\lambda = \eta/L_s$. The friction coefficient for the rectangular asperities is 1.55×10^5 N s m⁻³, while those for the triangular and sigmoidal asperities are $\sim 2.8 \times 10^4$ N s m⁻³ (Table 2). Owing to the friction of the wall and viscosity of the fluid, the shale gas velocity profile has a parabolic shape.

The volumetric fluxes of methane as a function of pressure and roughness geometry are compared in Fig. 6(f). Flux values are calculated from Eq. (3), and the relative contribution of the adsorbed layer to the overall flux is calculated from $P = 100\% \times \sum (v_i \rho_i)_{ads} / \{\sum (v_i \rho_i)_{ads} + \sum (v_i \rho_i)_{bulk}\}$ (Kunert and Harting, 2007). The entire

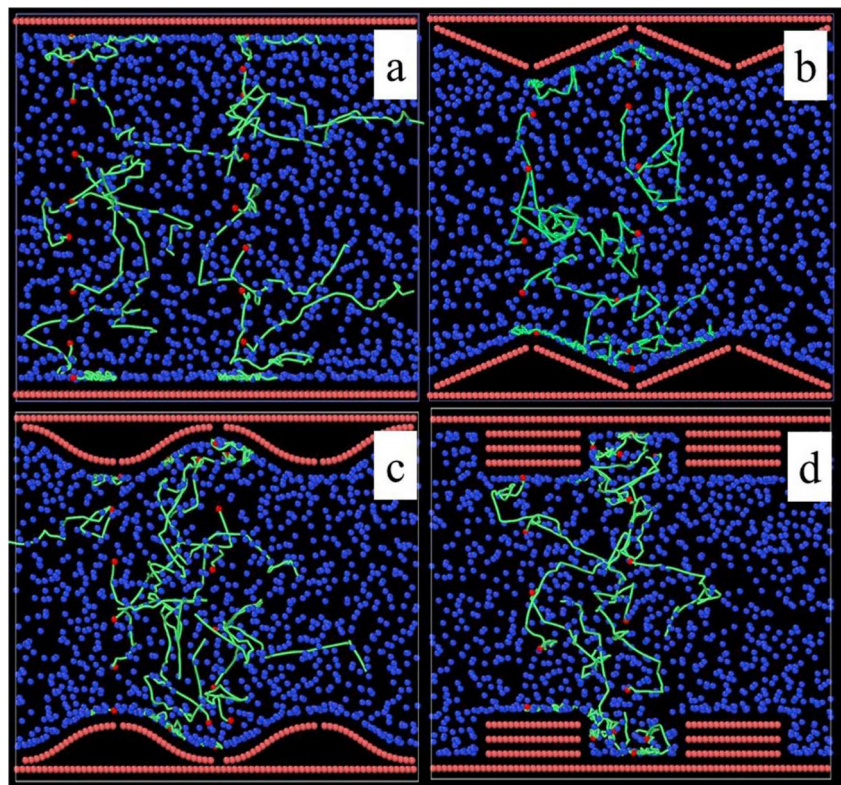


Fig. 7. Trajectory of methane molecules in nanopores over 10 ps after 15 ns of the NEMD simulation for (a) smooth nanopores, (b) nanopores with triangular asperities, (c) nanopores with sigmoidal asperities, and (d) nanopores with rectangular asperities.

methane flux occurring within 8 Å of each surface is attributed to the adsorbed (double) layers. After the calculation, we can see that the average flux obtained from the HP equation increases linearly as a function of external force (Fig. 6(f)). For the triangular asperities, the relationship between the flux and external force can be expressed as $f_{\text{triangular}} = (8.07 \times 10^6)F - 102$. For the sigmoidal and rectangular asperities, the relationship can be expressed as $f_{\text{sigmoidal}} = (8.47 \times 10^6)F - 157$ and $f_{\text{rectangular}} = (5.69 \times 10^6)F + 55$, respectively. Interestingly, the relative percentage contribution of the adsorbed methane to the overall flux (P) does not vary with external applied force, indicating that the increase in flux in this layer scales directly with the increased flux in the pore interiors. With the increase of force, both the increased flux and the contribution of the adsorbed layer are in the order of sigmoidal \geq triangular $>$ rectangular. For pores with sigmoidal asperities, the contribution of the adsorbed layer to the total methane flux ranges from 30.6% to 34.1%, while it ranges from only 20.2%–24.9% for pores with rectangular asperities. We ascribe these differences primarily to the different densities and amounts of slip flow in the adsorbed layers. Even though the boundary speed is less than the maximum speed by a factor of 2 or 3 in all cases, the adsorption layer still contributes nearly 20%–30% of the total flux in these narrow pores (Kazemi and Takbiri-Borjeni, 2016c; Wu and Zhang, 2016). In a real shale pore system, the morphology of the nanopore wall is expected to be much more complex and may resemble a combination of these geometries.

To compare the relative mobility of methane molecules in the various pore geometries, the trajectory of methane in different nanopores is studied. For the roughened pores, trajectories are illustrated for NEMD simulations under an applied force of 0.001 kcal mol⁻¹ Å⁻¹. The speed in the ultra-smooth nanopore is too high for visualization under this condition; therefore, a force of 0.0001 kcal mol⁻¹ Å⁻¹ is used

instead to study the methane trajectory in smooth nanopores. As we can see from Fig. 7(a), the trajectories in the adsorbed double layer are extremely different from the trajectories in the center of the nanopore. Because of the high density of the adsorbed layer and adsorption affinity of the wall, CH₄ molecules in this layer are more likely to collide with other adsorbed particles and tend to move along the surface without entering the bulk interior area (Li et al., 2016). Therefore, the direction of single methane molecules can change frequently along the wall surface. However, the average fluid mainstream flow direction is consistent with the pressure gradient direction. These findings are in agreement with other research (Li et al., 2016) in which the adsorbed layers tend to move along the solid surface.

On roughened nanopore surfaces (Fig. 7(b)–(d)), more methane is trapped between the rough units (He et al., 2016), as discussed above and illustrated in Fig. A2 (see Appendix). In addition to the higher possibility of particle–particle collision, methane in the cavities or grooves between asperities tends to collide with rough walls, which may cause intense backflow; meanwhile, the mainstream speed decreases very quickly owing to the momentum exchange between trapped and free methane gas. Especially for the rectangular asperities (Fig. 7(d)), where the rough walls are perpendicular to the mainstream flow direction, the trapped methane is in a stationary state, and the trajectory is completely distorted. Fluid flow is most severely obstructed in the rectangular roughness geometry because methane molecules have more difficulty in escaping the vertically walled cavities.

3.3. Gas flux as a function of relative roughness and other influential factors

In this section, we investigate the effects of surface roughness, pore diameter, and periodicity on shale gas flow by using nanopores with a

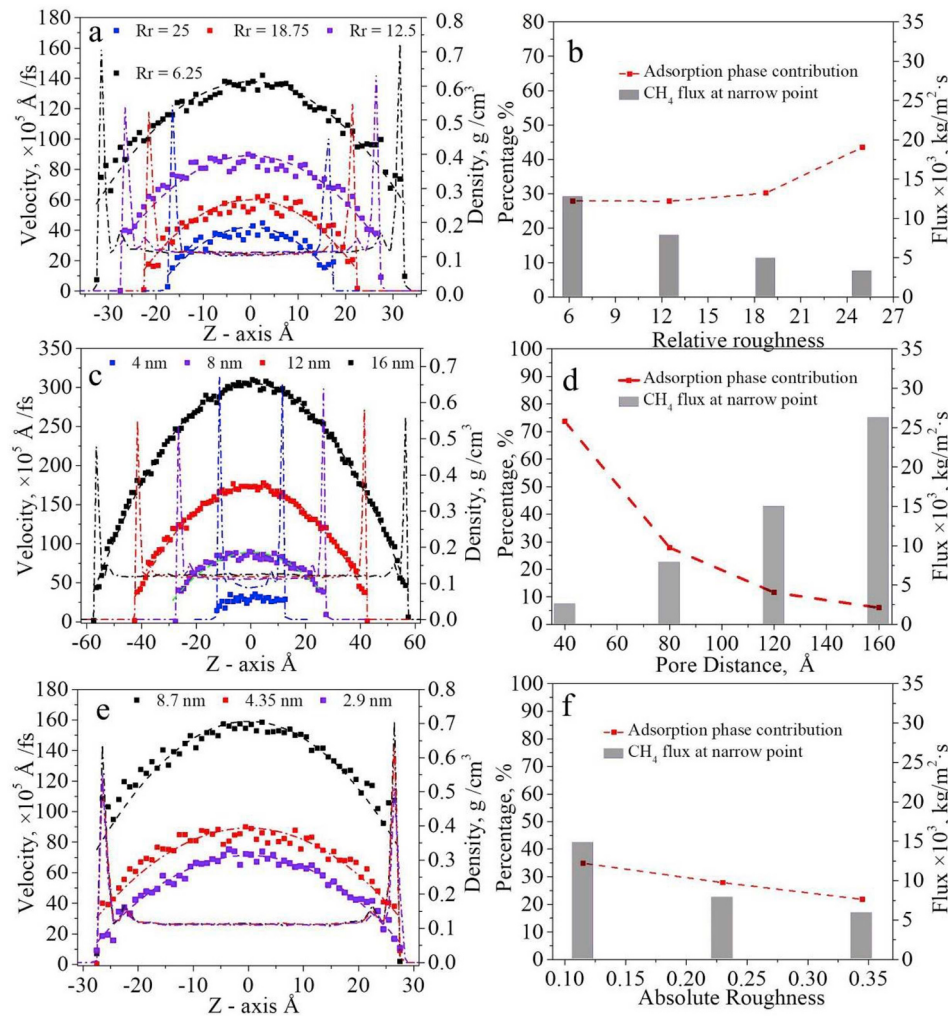


Fig. 8. Density (colored dash-dotted lines), velocity (colored solid dots), and flux profiles (rectangular bar chart) for different (a, b) relative roughness, (c, d) pore diameters, and (e, f) periodicity values. The fitting lines obtained from the modified HP equation are shown by dashed lines. The adsorption-layer contribution to the shale gas flux is plotted along with the average flux.

triangular roughness geometry. The pressure gradient is set as $0.001 \text{ kcal mol}^{-1} \text{ Å}^{-1}$ for all simulations. The speed and density profiles at the narrowest point are plotted in Fig. 8(a), (c), and (e), and the mass fluxes obtained from Eq. (4) are shown in Fig. 8(b), (d), and 8(f). According to the results of the simulations at different values of relative roughness (R_r), the maximum flow velocity decreases rapidly from 149 to 50 m/s with the increase of relative roughness from 6.3% to 25%. The flux is as high as $1.27 \times 10^4 \text{ kg m}^{-2} \text{ s}^{-1}$ at the lowest value of R_r equal to 6.25%. Increasing R_r to 25% decreases the methane flux by $\sim 36.8\%$ to $3.25 \times 10^3 \text{ kg m}^{-2} \text{ s}^{-1}$. As previously reported, gas flux is mainly related to the speed and density distribution of gas in the pores (Jin and Firoozabadi, 2015). With the increase of R_r , more methane is trapped in the grooves between the asperities. The density distribution inside the cavities increases with R_r , as shown in Fig. A4 (see Appendix). Consequently, the increased confinement of methane due of adsorption causes the average flux to decrease, and the contribution of the adsorbed layer to this flux, which is related to the boundary speed and density, also decreases from 43.5% to 27.9%.

The influence of pore diameter on shale gas flow is studied at a constant R_r of 12.5%. Fig. 8(c) shows that the mainstream speed increases with increasing pore size. The maximum speed of methane in the smallest pore (40.5 m s^{-1}) is much lower than that in the largest

pore (346 m s^{-1}), while the boundary speed is nearly the same in both cases. When the pore diameter is decreased to 4 nm, the velocity becomes nearly uniform across the pore width. We attribute this observation to the fact that, in this case, the pore diameter approaches the molecular mean free path, and the flow regime is dominated by molecular diffusion rather than slip flow, which cannot be described by the modified HP equation (Kou et al., 2016). Calculating the flux with the HP equation for such a pore can lead to very large errors. Therefore, the average flux is obtained from $f_2 = (\sum_{i \in m, \text{bin}} \hat{\rho}_i \hat{v}_i)/m$, where m is the number of bins (equal to 36 here). Not surprisingly, the flux increases with increasing pore diameter (Fig. 8(d)); the widest pore (16 nm) has the highest flux ($2.6 \times 10^4 \text{ kg m}^{-2} \text{ s}^{-1}$) and the narrowest pore (4 nm) has the lowest flux ($2.5 \times 10^3 \text{ kg m}^{-2} \text{ s}^{-1}$). Conversely, the percentage contribution of the adsorbed layers to the overall flux decreases with increasing pore diameter, reaching 73.7% for the narrowest 4-nm pore. In this case, nearly half the volume of the pore is in an adsorbed layer. When the pore size increased to 16 nm, the contribution is dramatically decreased to 6.1%.

The absolute roughness of a pore depends on the height of the asperities and their periodicity (Sun and Faghri, 2003). To better understand the effect of absolute roughness on shale gas flow, the roughness is set as 0.1149, 0.2299, and 0.3448 by keeping the height of each

asperity constant at 1 nm and setting the periodicity to 8.7, 4.35, and 2.9 nm. The obtained velocity distributions in whole pores are shown in Figs. A3(c1)–(c3) (see Appendix), and the speed and density profiles at the narrowest point are plotted in Fig. 8(e). Because the velocity profile has a parabolic shape, by using viscosity and slip length, we obtain the following friction coefficients: 1.15×10^4 , 2.80×10^4 , and 6.75×10^4 (Ns)/m³. Consequently, the flux in Fig. 6(f) decreases from 1.48×10^4 to 5.86×10^3 kg/m²s, which we mainly ascribe to the reduced space in the grooves. The collision frequency between the trapped methane gas and the wall also becomes stronger as a result. The typical contribution of the adsorbed layer is 20%–30% and exhibits a linear decrease with roughness, which in this case is the same as the variation of the average flux.

Compared to the smooth pores in Fig. A1 (see Appendix), we can see that a high relative roughness dramatically decreases the flow speed and gas flux while maintaining a constant contribution from slip flow. We attribute this finding to CH₄ confinement in cavities, which decouples slip flow from flow in the pore interior. Moreover, we find that both the overall flux and the boundary speed of the adsorbed layer scale linearly with the applied force, causing the relative contribution of slip flow to the overall flux to be independent of the pressure gradient. Although the geometry of rough units does influence the shale gas flux, the influence is relatively weak compared with the other factors considered here. We find that, for gas flow in high-relative-roughness nanopores, the pore size is the most important factor controlling the overall flux and the relative contribution of the adsorbed layer, similar to smooth nanopores (Kazemi and Takbiri-Borujeni, 2016c). For pores < 4 nm in diameter, the flow regime is dominated by molecular diffusion rather than slip flow, which cannot be described by the modified HP equation.

4. Conclusions

We used EMD and NEMD simulations to study shale gas flux in organic nanopores with a high relative roughness over a range of pressure gradients, pore diameters, roughness geometries (i.e., triangular, sigmoidal, and rectangular asperities), and roughness periodicities. The result shows that the flow regime changes from slip flow to

Appendix

To compare the results obtained from rough nanopores with those from smooth nanopores, the shale gas flow in smooth nanopores is studied with an external force in the range of 0.0001–0.00035 kcal mol⁻¹ Å⁻¹ (Kazemi and Takbiri-Borujeni, 2016a; Kazemi and Takbirborujeni, 2016b). The MD simulation process is the same as that for rough nanopores. Because of the completely smooth wall, the mainstream speed is much higher than the speed of the shale gas flow in rough nanopores under the same condition. If we use the same force of 0.001 kcal mol⁻¹ Å⁻¹ that was used for the case of rough nanopores, the mainstream speed is much higher than the molecular thermal velocity, which is 660 m/s as calculated with $c = \sqrt{8RT/(\pi M)}$. Only the displacement in the x direction can be observed, which is not consistent with the spurious dynamic state exhibited by the thermal motion rule. Therefore, the pressure gradients we used here are much smaller than the force used in the rough nanopores. The obtained speed distribution map shown in Fig. A1(a) indicates that the velocity profile is nearly flat. This is different from continuum flow and viscosity flow. According to the density distribution map in Fig. A1(b), we can see that two adsorption layers covered the surface with a density of ~0.8 g/cm³. The single thickness of the adsorption layer approaches 0.4 nm, which is determined by the dynamic diameter of methane (0.35 nm).

The speed of shale gas flow under different pressure gradients is shown in Fig. A1(c). Here, we use $f_2 = (\sum_{i \in m, bin} \hat{\rho}_i \hat{v}_i)/m$ to calculate the flux and compare our calculation results with previously published simulation results to validate our model. Because of the higher density along the surface and the same speed across the pore, as we can see from Fig. A1(d) that the flux near the surface is higher than the bulk-phase flux. With the increase of the pressure gradient, the average flux maintains a linear increase before the pressure gradient reaches 0.0003 kcal mol⁻¹ Å⁻¹. However, when the external force is > 0.00035 kcal mol⁻¹ Å⁻¹, the average flux increases very quickly because the speed is comparable to the thermal speed. Particle-particle and particle-wall interactions do not play a dominant role in shale gas flow in nanopores. The mainstream speed increases with the simulation time and pressure gradient, as reported in a previous study (Qin and He, 2016), and the contributions of the adsorption layer to the shale gas flux for different pressure gradients are nearly the same at 34%. Kazemi and Takbirborujeni studied the methane flow in 4-nm organic nanopores by using the same method and showed that the contribution of the adsorption layer is 42%–53% (Kazemi and Takbirborujeni, 2016b). This value is higher than our result, but the pore distance they used is 8 nm. Thus, the contribution of adsorption increases as the pore size decreases.

molecular diffusion at very small pore diameters. Consequently, methane fluxes cannot be suitably described by the modified HP equation when the pore size is < 4 nm. According to molecular trajectories, we find that the adsorbed layer moves along the wall, resulting in often significant contributions from slip flow in these organic nanopores. The relative contribution of slip flow to the overall gas flux varies with the geometry of the asperities (sigmoidal ≥ triangle > rectangle), pore diameters, and absolute roughness but not with the magnitude of the pressure gradient. Typical contributions of the adsorption layer caused by slip flow are in the range of 20%–40%, but they can be as high as 74% when the pore size is decreased to 4 nm and as low as 6.1% when the pore size is increased to 16 nm. Our findings indicate that, in high-relative-roughness nanopores, the pore size is likely to be the dominant factor governing the overall CH₄ gas flux, while the geometry of the asperities and the absolute roughness of the pores are of secondary importance. To accurately predict pore-scale gas flow in kerogen-rich shales, these key variables must be explicitly taken into account.

Notes

The authors declare no competing interest.

Acknowledgements

The authors gratefully acknowledge the financial support from the State Key Research Development Program of China (Grant No. 2016YFC0600705), the National Major Project for Science and Technology (Grant No. 2017ZX05049003-006), the National Natural Science Foundation of China (Grant Nos. 51674251, 51727807, and 51374213), the National Natural Science Foundation for Distinguished Young Scholars of China (Grant No. 51125017), and the Fund for Innovative Research Teams Sponsored by National Ten-Thousand Talents Program (Grant No. 2018). Additionally, Jian He would like to acknowledge the China Scholarship Council (CSC) for funding his study at the Lawrence Berkeley National Laboratory and the University of California, Berkeley. The authors would like to thank Sen Wang, Jun Zhang, and Xin Zheng for valuable discussions about the MD simulations.

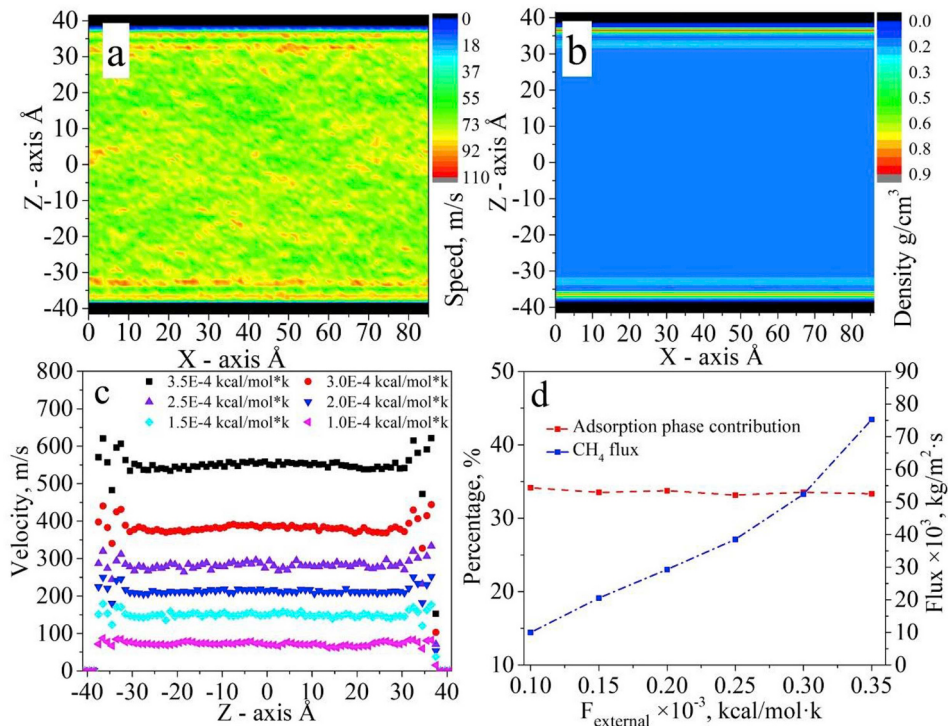


Fig. A1. Methane flow in smooth nanopores with an external force equal to $0.0001 \text{ kcal mol}^{-1} \text{ \AA}^{-1}$: (a) velocity distribution map; (b) density distribution map. (c) Speed profiles across the nanopores at different external forces. (d) Average shale gas flux and the adsorption contribution to average flux for different external forces.

The density distribution of methane is studied in nanopores with different surface structures. As shown in Fig. A2, the density at the center of nanopores is uniform along the surface structure, while the shapes of adsorption layers are nearly the same as the surface geometries. There are two clear adsorption layers along the surface that have been observed in many papers (e.g. Mosher et al., 2013), and the highest density usually occurs at the bottom points, which are also the narrowest points between two rough units in the x direction. The density decreases in the order of rectangular > triangular > sigmoidal, which is opposite to the order of velocity distribution. This may be the result of a higher friction coefficient, which causes more methane to be trapped between the rough units. However, for rectangular units, the cliff surface parallel to the z axis exhibits a weaker adsorption ability. The density of the adsorption layer along the cliff faces in the rectangular structure surface is also less than that in other surfaces.

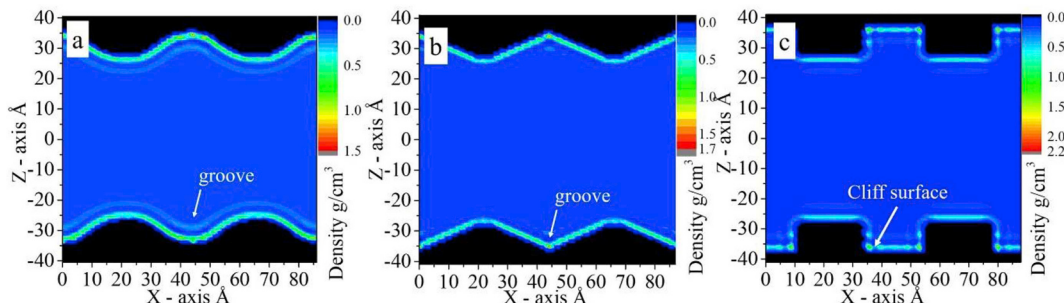


Fig. A2. Density distribution maps of methane in rough nanopores with (a) triangular, (b) sigmoidal, and (c) rectangular surface structures. The pressure gradients are the same at $0.001 \text{ kcal mol}^{-1} \text{ \AA}^{-1}$.

Figure A3 illustrates the velocity distribution of shale gas flow in organic nanopores with different surface roughnesses, pore distances, and periodicities. The pore distance is set as 16, 12, 8, and 4 nm with the same relative roughness value in Fig. A3(a). From the speed maps, we can see that the speed decreases dramatically as the nanopore distance decreases. When the pore size is $< 4 \text{ nm}$, the speed in the center pore is identical to the boundary speed. Further, the shale gas flow changes from slip flow to molecular diffusion (Kou et al., 2016). With the increase of relative roughness, the absolute roughness is also increased. When the roughness is < 6.25 , the maximum speed reaches 150 m/s. With the increase of relative roughness, the speed is decreased from 150 to 40 m/s while the morphology of the speed distribution across the z axis still exhibits a spindle shape. The shale gas flow can still be described by the modified HP equation. In Fig. A3(c), with the decrease of periodicity, the absolute roughness is increased. Especially, when the periodicity is $> 8.7 \text{ nm}$, the maximum speed is almost twice the speed in other situations.

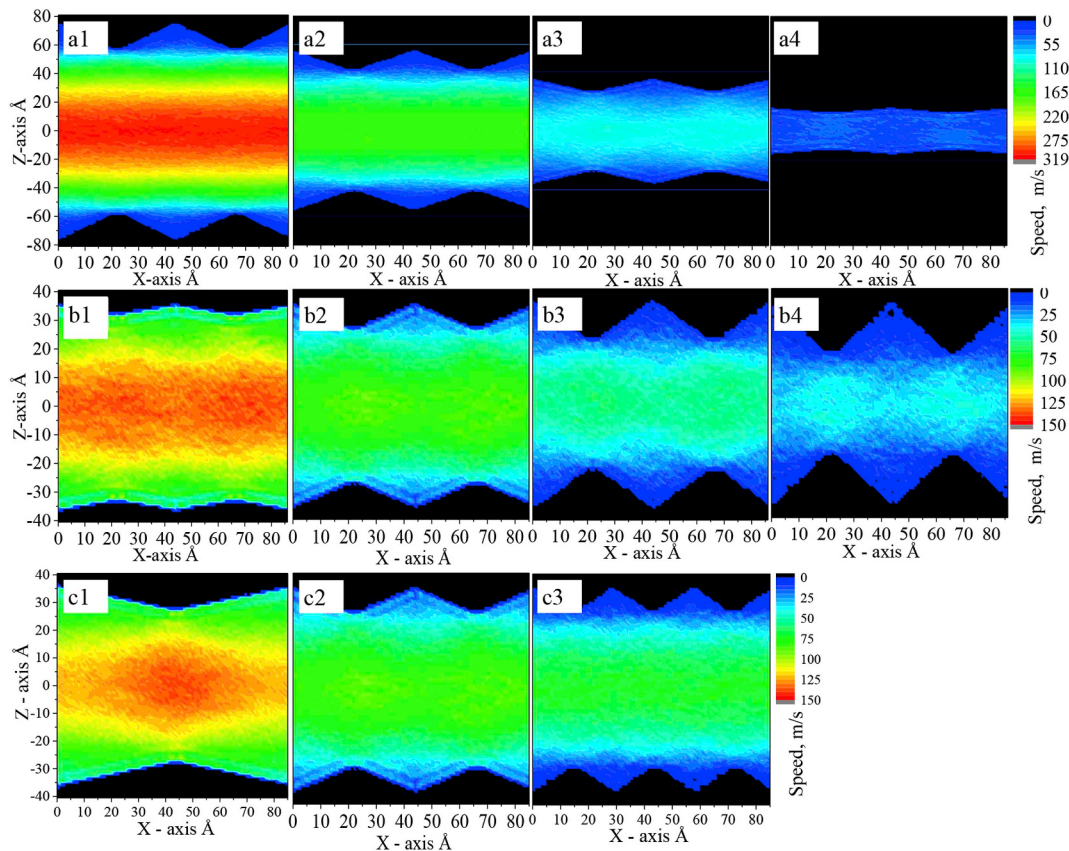


Fig. A3. Velocity distribution maps in rough nanopores with pore distances of (a1) 16 nm, (a2) 12 nm, (a3) 8 nm, and (a4) 4 nm. The effect of relative roughness values of (b1) 6.25%, (b2) 8.33%, (b3) 12.5%, and (b4) 25% on the velocity distribution maps shown. Velocity distribution maps in nanopores with different periodicities: (c1) 8.7 nm, (c2) 4.35 nm, and (c3) 2.9 nm.

The effect of relative roughness on the density distribution is shown in Fig. A4. As we can see from Fig. A4, the density in the center of the nanopores is very uniform, which is the same as in other situations. This phenomenon is not changed with the growth of rough units, while the shape of the adsorption layer is changed with the surface structure. Further, the density distribution inside the cavities increases with the relative roughness. The highest density in the cavities reaches 3.0 g/cm^3 , while the density in low-relative-roughness nanopores is only 1.3 g/cm^3 . However, all the maximum density values in the rough nanopores are higher than that in the smooth nanopores, which is $\sim 0.8 \text{ g/cm}^3$. This trend is opposite to that of the velocity distribution, which has been explained in Fig. A3.

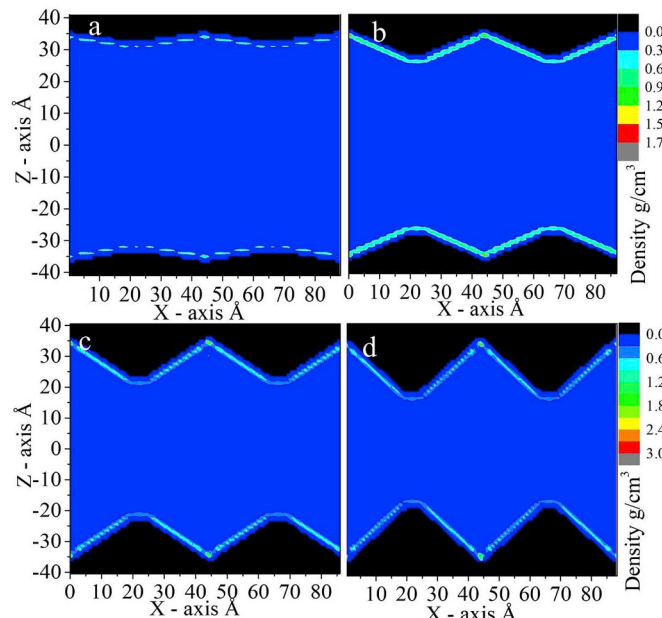


Fig. A4. Density distribution maps of methane in 8-nm nanopores with relative roughnesses of (a) 6.25, (b) 12.5, (c) 18.75, and (d) 25. During the simulation, the pressure is kept constant at $0.001 \text{ kcal mol}^{-1} \text{ Å}^{-1}$.

Appendix A. Supplementary data

Supplementary data to this article can be found online at <https://doi.org/10.1016/j.jngse.2018.12.010>.

References

- Bousige, C., Ghimbeu, C.M., Vix-Guterl, C., Pomerantz, A.E., Suleimenova, A., Vaughan, G., Garbarino, G., Feygenson, M., Wildgruber, C., Ulm, F.J., Pellenq, R.J., Coasne, B., 2016. Realistic molecular model of kerogen's nanostructure. *Nat. Mater.* 15, 576–582.
- Cao, B.Y., Chen, M., Guo, Z.-Y., 2006. Effect of surface roughness on gas flow in micro-channels by molecular dynamics simulation. *Int. J. Eng. Sci.* 44, 927–937.
- Castez, M.F., Winograd, E.A., Sánchez, V.M., 2017. Methane flow through organic-rich nanopores: the key role of atomic-scale roughness. *J. Phys. Chem. C* 121, 28527–28536.
- Chae, K., Huang, L., 2016. Computational study of pressure-driven methane transport in hierarchical nanostructured porous carbons. *J. Chem. Phys.* 144, 044708.
- Chalmers, G.R., Bustin, R.M., Power, I.M., 2012a. Characterization of gas shale pore systems by porosimetry, pycnometry, surface area, and field emission scanning electron microscopy/transmission electron microscopy image analyses: examples from the Barnett, Woodford, Haynesville, Marcellus, and Doig units. *AAPG Bull.* 96, 1099–1119.
- Chalmers, G.R.L., Ross, D.J.K., Bustin, R.M., 2012b. Geological controls on matrix permeability of Devonian gas shales in the horn river and liard basins, northeastern British Columbia, Canada. *Int. J. Coal Geol.* 103, 120–131.
- Docherty, S.Y., Nicholls, W.D., Borg, M.K., Lockerby, D.A., Reese, J.M., 2013. Boundary conditions for molecular dynamics simulations of water transport through nanotubes. *P. I. Mech. Eng. C - J. MEC.* 228, 186–195.
- Dong, T., Harris, N.B., Ayrancı, K., Twemlow, C.E., Nassichuk, B.R., 2015. Porosity characteristics of the Devonian Horn River shale, Canada: insights from lithofacies classification and shale composition. *Int. J. Coal Geol.* 141–142, 74–90.
- Evans, D.J., Holian, B.L., 1985. The nose-hoover thermostat. *J. Chem. Phys.* 83, 4069–4074.
- Firouzi, M., Wilcox, J., 2013. Slippage and viscosity predictions in carbon micropores and their influence on CO₂ and CH₄ transport. *J. Chem. Phys.* 138, 064705.
- Gao, Q., Zhu, Y., Ruan, Y., Zhang, Y., Zhu, W., Lu, X., et al., 2017. Effect of adsorbed alcohol layers on the behavior of water molecules confined in a graphene nanoslit: a molecular dynamics study. *Langmuir* 42, 11467–11474.
- Greathouse, J.A., Teich-McGoldrick, S.L., Allendorf, M.D., 2015. Molecular simulation of size-selective gas adsorption in idealised carbon nanotubes. *Mol. Simulat.* 41, 1388–1395.
- He, S., Ning, Y., Chen, T., Liu, H., Wang, H., Qin, G., 2016. Estimation of transport diffusivity of natural gas in organic matter using molecular dynamics simulation. In: SPE Low Perm. Symposium.
- Humphrey, W., Dalke, A., Schulten, K., 1996. VMD: Visual Molecular Dynamics.
- Islam, A., Patzek, T., 2014. Slip in natural gas flow through nanoporous shale reservoirs. *J. Unconv. Oil. Gas Resour.* 7, 49–54.
- Javadpour, F., McClure, M., Naraghi, M.E., 2015. Slip-corrected liquid permeability and its effect on hydraulic fracturing and fluid loss in shale. *Fuel* 160, 549–559.
- Jiang, C., Ouyang, J., Wang, L., Liu, Q., Wang, X., 2017. Transport properties and structure of dense methane fluid in the rough nano-channels using non-equilibrium multiscale molecular dynamics simulation. *Int. J. Heat Mass Tran.* 110, 80–93.
- Jin, Z., Firoozabadi, A., 2015. Flow of methane in shale nanopores at low and high pressure by molecular dynamics simulations. *J. Chem. Phys.* 143, 104315.
- Jin, Z., Firoozabadi, A., 2016. Phase behavior and flow in shale nanopores from molecular simulations. *Fluid Phase Equilibr.* 430, 156–168.
- Kannan, S.K., Todd, B.D., Hansen, J.S., Daivis, P.J., 2012. Slip length of water on graphene: limitations of non-equilibrium molecular dynamics simulations. *J. Chem. Phys.* 136, 024705.
- Kaufhold, S., Grathoff, G., Halisch, M., Plotze, M., Kus, J., Ufer, K., Dohrmann, R., Ladage, S., Ostertag-Henning, Ch., 2016. Comparison of methods for the determination of the pore system of a potential German gas shale. In: The Clay Minerals Society Workshop Lectures Series 21, pp. 27.
- Kazemi, M., Takbiri-Borjene, A., 2016a. Flow of gases in organic nanoscale channels: a boundary-driven molecular simulation study. *Energy Fuels* 30, 8156–8163.
- Kazemi, M., Takbiri-Borjene, A., 2016b. Flow of gases in slit shaped organic nanopores of shale: a boundary-driven molecular simulation study. In: SPE Low Perm. Symposium.
- Kazemi, M., Takbiri-Borjene, A., 2016c. Non-equilibrium molecular dynamics simulation of gas flow in organic nanochannels. *J. Nat. Gas Sci. Eng.* 33, 1087–1094.
- Kou, R., Alafnan, S.F.K., Akkutlu, I.Y., 2016. Multi-scale analysis of gas transport mechanisms in kerogen. *Transport Porous Media* 116, 493–519.
- Kunert, C., Harting, J., 2007. Roughness induced boundary slip in microchannel flows. *Phys. Rev. Lett.* 99.
- Li, Z.Z., Min, T., Kang, Q., He, Y.L., Tao, W.Q., 2016. Investigation of methane adsorption and its effect on gas transport in shale matrix through microscale and mesoscale simulations. *Int. J. Heat Mass Tran.* 98, 675–686.
- Leggesse, E.G., Chen, C.L., Jiang, J.C., 2016. Lithium diffusion in graphene and graphite: effect of edge morphology. *Carbon* 103, 209–216.
- Loucks, R.G., Reed, R.M., Ruppel, S.C., Jarvie, D.M., 2009. Morphology, genesis, and distribution of nanometer-scale pores in siliceous mudstones of the Mississippian Barnett Shale. *J. Sediment. Res.* 79, 848–861.
- Mondello, M., Grest, G.S., 1997. Viscosity calculations of n-alkanes by equilibrium molecular dynamics. *J. Chem. Phys.* 106, 9327–9336.
- Moody, L.F., 1944. Friction factors for pipe flow. *Trans. ASME* 66, 671–684.
- Mosher, K., He, J., Liu, Y., Rupp, E., Wilcox, J., 2013. Molecular simulation of methane adsorption in micro- and mesoporous carbons with applications to coal and gas shale systems. *Int. J. Coal Geol.* 109, 36–44.
- Noorani, H., Toghraie, D., Azimian, A.R., 2013. The effects of surface roughness geometry of flow undergoing Poiseuille flow by molecular dynamics simulation. *Heat Mass Tran.* 50, 95–104.
- Oliphant, T.E., 2007. Python for scientific computing. *Comput. Sci. Eng.* 9, 10–20.
- Ou, J., Perot, B., Rothstein, J.P., 2004. Laminar drag reduction in microchannels using ultrahydrophobic surfaces. *Phys. Fluids* 16, 4635–4643.
- Plimpton, S., 1993. Fast parallel algorithms for short-range molecular dynamics. *J. Comput. Phys.* 117, 1–19.
- Pit, R., Hervet, H., Leger, L., 2000. Direct experimental evidence of slip in hexadecane: solid interfaces. *Phys. Rev. Lett.* 85, 980–983.
- Qin, G., He, S., 2016. Molecular dynamics simulation on modeling shale gas transport and storage mechanisms in complex nano-pore structure in organic matters. *Unconventional Resources Technology Conference* 2465–2477.
- Rahmatipour, H., Azimian, A.-R., Atlashian, O., 2017. Study of fluid flow behavior in smooth and rough nanochannels through oscillatory wall by molecular dynamics simulation. *Physica A* 465, 159–174.
- Schmatko, T., Hervet, H., Léger, L., 2006. Effect of nanometric-scale roughness on slip at the wall of simple fluids. *Langmuir* 22, 6843–6850.
- Sharma, A., Namsani, S., Singh, J.K., 2014. Molecular simulation of shale gas adsorption and diffusion in inorganic nanopores. *Mol. Simulat.* 41, 414–422.
- Shen, V.K., Siderius, D.W., Krekelberg, W.P., Hatch, H.W. (Eds.), 2011. NIST Standard Reference Simulation Website, NIST Standard Reference Database Number 173. National Institute of Standards and Technology, Gaithersburg MD 20899. <http://doi.org/10.18434/T4M88Q>.
- Skoulidas, A.I., Ackerman, D.M., Johnson, J.K., Sholl, D.S., 2002. Rapid transport of gases in carbon nanotubes. *Phys. Rev. Lett.* 89, 185901.
- Stukowski, A., 2010. Visualization and analysis of atomistic simulation data with OVITO—the Open Visualization Tool. *Model. Simul. Mater. Sci.* 18, 015012.
- Such, P., Cicha-Szot, R., Dudek, L., 2016. Fluid flow through nanopore space: discussion and proposition of a model for Polish shales. *Nafta-Gaz* 72, 779–784.
- Sui, H., Yao, J., 2016. Effect of surface chemistry for CH₄/CO₂ adsorption in kerogen: a molecular simulation study. *J. Nat. Gas Sci. Eng.* 31, 738–746.
- Suk, M.E., Aluru, N.R., 2013. Molecular and continuum hydrodynamics in graphene nanopores. *RSC Adv.* 24, 9365.
- Sun, H., Faghri, M., 2003. Effect of surface roughness on nitrogen flow in a microchannel using the direct simulation Monte Carlo method. *Numer. Heat Tr. A-Appl.* 43, 1–8.
- Tang, X., Ripepi, N., Stadie, N.P., Yu, L., 2017. Thermodynamic analysis of high pressure methane adsorption in Longmaxi shale. *Fuel* 193, 411–418.
- Wang, S., Feng, Q., Javadpour, F., Yang, Y.-B., 2016a. Breakdown of fast mass transport of methane through calcite nanopores. *J. Phys. Chem. C* 120, 14260–14269.
- Wang, S., Javadpour, F., Feng, Q., 2016b. Fast mass transport of oil and supercritical carbon dioxide through organic nanopores in shale. *Fuel* 181, 741–758.
- Wang, S., Javadpour, F., Feng, Q., 2016c. Molecular dynamics simulations of oil transport through inorganic nanopores in shale. *Fuel* 171, 74–86.
- Wang, S., Feng, Q., Zha, M., Javadpour, F., Hu, Q., 2018. Supercritical methane diffusion in shale nanopores: effects of pressure, mineral types, and moisture content. *Energy Fuels* 32, 169–180.
- Wu, H.A., Chen, J., Liu, H., 2015. Molecular dynamics simulations about adsorption and displacement of methane in carbon nanochannels. *J. Phys. Chem. C* 119, 13652–13657.
- Wu, T., Zhang, D., 2016. Impact of adsorption on gas transport in nanopores. *Sci. Rep.* 6, 23629.
- Xie, J.F., Cao, B.Y., 2016. Effect of various surface conditions on nanochannel flows past permeable walls. *Mol. Simulat.* 43, 1–11.
- Yan, Y., Li, C., Dong, Z., Fang, T., Sun, B., Zhang, J., 2017. Enhanced oil recovery mechanism of CO₂ water-alternating-gas injection in silica nanochannel. *Fuel* 190, 253–259.
- Yao, J., Sun, H., Fan, D.Y., Wang, C.C., Sun, Z.X., 2013. Numerical simulation of gas transport mechanisms in tight shale gas reservoirs. *Petrol. Sci.* 10, 528–537.
- Yen, T.H., 2013. Molecular dynamics simulation of fluid containing gas in hydrophilic rough wall nanochannels. *Microfluid. Nanofluidics* 17, 325–339.